Applied Catalysis A: General 369 (2009) 15–26

Contents lists available at ScienceDirect

Applied Catalysis A: General

journal homepage: www.elsevier.com/locate/apcata

# Surface properties and catalytic behavior of Ru supported on composite $La_2O_3$–$SiO_2$ oxides

B.M. Faroldi, E.A. Lombardo, L.M. Cornaglia *

*Instituto de Investigaciones en Catálisis y Petroquímica (FIQ, UNL-CONICET), Santiago del Estero 2829, 3000-Santa Fe, Argentina*

ARTICLE INFO

*Article history:*
Received 2 June 2009
Received in revised form 31 July 2009
Accepted 13 August 2009
Available online 21 August 2009

*Keywords:*
Binary supports
Ru
Hydrogen production
XPS
ISS

ABSTRACT

Binary $La_2O_3$–$SiO_2$ supports were employed to obtain active, stable Ru catalysts with high dispersions for the dry reforming of methane. Supports with 15, 27, 40 and 50 wt.% of $La_2O_3$ were prepared by incipient wetness impregnation on $SiO_2$. The Ru loading was 0.6 wt.% for all catalysts. The solids were evaluated in a fixed-bed reactor under differential conditions. Previously, they were reduced at either 673 or 823 K. The most active catalyst was Ru/$La_2O_3$(50)–$SiO_2$. All the uncalcined formulations were stable after 100 h on stream.

XRD, CO chemisorption, TPR, XPS, ISS and CO adsorption monitored by FTIR were employed to characterize the catalysts and the Ru species. XRD showed the presence of $La_2Si_2O_7$ with low crystallinity in all the supports. By means of XPS and ISS, the formation of a surface $La_2Si_2O_7$ phase was suggested for samples containing $La_2O_3$ up to 40 wt.%. Higher contents could lead to surface $La_2O_3$ particle growth.

The $TOF_{CH_4}$ values showed a minimum for the Ru/$La_2O_3$(40)–$SiO_2$ solid in agreement with a lower metal–support interaction. The Ru/$La_2O_3$(50)–$SiO_2$ catalyst exhibited the highest $TOF_{CH_4}$ for both reduction treatments. The differences in thermal stability of the CO adsorbed species on Ru supported on silica or on binary $La_2O_3$–$SiO_2$ supports sustain that the presence of lanthanum influences the metal–support interaction and metal dispersion.

© 2009 Elsevier B.V. All rights reserved.

## 1. Introduction

Hydrogen production through the dry reforming of methane could contribute to the use of $H_2$ as an alternative fuel, thus avoiding the constraints imposed by the storage and distribution of this gas. Both methane and carbon dioxide contribute to the greenhouse effect; consequently the $CO_2$ reforming of methane could have an important environmental implication. One of the main problems for the preparation of effective reforming catalysts is the deactivation due to coke formation. In the presence of noble metals and an adequate support, coke formation can be attenuated. Dispersing the active metal on a high surface area solid and using the right promoters could improve catalyst activity and stability.

The noble metal-based catalysts like rhodium and ruthenium are less sensitive to coke deposits than the nickel-based ones. The rate of carbon formation was found to be much lower in noble metals, which was ascribed to a lower dissolution of carbon in these metals [1].

As a bonus, ruthenium is much cheaper than rhodium. Several studies [2–11] have shown the high activity of Ru-containing formulations. The activity and selectivity of Ru catalysts greatly depend on the oxidation state [9] of the metal, which can change depending on both the reaction conditions and the support used.

Support effects on the catalytic behavior of Ru catalysts were investigated by various authors [2–7]. Nagaoka et al. [6] reported that the activity on the supported catalysts decreases in the order $Ru/MgO > Ru/Al_2O_3 > Ru/TiO_2 > Ru/SiO_2$. It seems to be in agreement with the basicity of the support, indicating that the $CO_2$ adsorption ability on the supports determine the catalytic activity. Besides, Ferreira-Aparicio et al. [3] found an active role of the support in $Ru/SiO_2$ and $Ru/Al_2O_3$, and proposed different reaction mechanisms for each catalyst. Bradford and Vannice [4] compared high dispersion catalysts (>50%) and found that the turnover frequencies decreased in the order $TiO_2 > Al_2O_3 \gg C$. However, other authors [5,7] reported no detectable effect of the nature of the support on the reaction rate. In this sense, Wei and Iglesia [5] reported that forward turnover rates were strongly influenced by Ru dispersion but were essentially insensitive to the identity of the support, although they did not use $La_2O_3$ as a carrier.

In La-based noble metal catalysts, we reported [10,12,13] a high stability attributed to the metal–support interaction. For Ru and

* Corresponding author. Tel.: +54 342 4536861; fax: +54 342 4536861.
*E-mail address:* lmcornag@fiq.unl.edu.ar (L.M. Cornaglia).

0926-860X/$ – see front matter © 2009 Elsevier B.V. All rights reserved.
doi:10.1016/j.apcata.2009.08.024

$Rh/La_2O_3$ solids, this interaction was very strong. However, when a composite $La_2O_3$–$SiO_2$ material was used as support, a weaker Rh–support interaction was observed [13].

The effect of lanthanum on the activity of metal supported catalysts has been recently reported [14,15]. The addition of $La_2O_3$ on the $Al_2O_3$ supported Pd catalyst resulted in an increase of the turnover rate for the steam reforming of methane assigned to changes in the Pd structure with Pd-site blockage [14]. In the case of Ni catalysts, the $La_2O_3$ content tuned the Ni particle sizes and Ni–H species amounts on the catalysts which led to a higher reforming activity [15].

The purpose of this work was to develop Ru-based catalysts supported on lanthanum binary supports to be applied in hydrogen production. We explored different thermal treatments to obtain active, stable catalysts for the dry reforming at moderate temperatures (823 K). The properties of the binary $La_2O_3$–$SiO_2$ supports and their influence in the nature of the Ru active sites have been studied by X-ray diffraction, $H_2$ and CO chemisorptions, temperature-programmed reduction, X-ray photoelectron spectroscopy, ion scattering spectroscopy and CO adsorption followed by Fourier transform infrared spectroscopy.

## 2. Experimental

### 2.1. Catalyst preparation

The $La_2O_3(x)$–$SiO_2$ supports were prepared by incipient wetness impregnation of $SiO_2$ (Aerosil 200, calcined at 1173 K) with lanthanum nitrate. Supports with 15, 27, 40 and 50 wt.% of $La_2O_3$ were prepared (nominal values). These values are indicated between parentheses. The samples were kept at room temperature for 2 h and then dried at 353 K overnight. The supports were calcined for 6 h at 823 K in flowing air. Metal deposition was performed by incipient wetness impregnation with $RuCl_3{\cdot}3H_2O$ as precursor compound followed by a drying step at 353 K. The amount of hydration water in the $RuCl_3$ was determined by thermogravimetric analysis. The nominal Ru loading was 0.6 wt.% for all catalysts.

### 2.2. Catalyst characterization

#### 2.2.1. Surface area

The BET (Brunauer, Emmett, and Teller) surface area was calculated from $N_2$ adsorption isotherms at liquid nitrogen temperature using a Quantachrome Autosorb automatic gas adsorption instrument. Prior to measurements, all samples were degassed at 423 K under a 0.13 Pa overnight.

#### 2.2.2. Metal dispersion

The metal dispersion of the fresh catalyst, following the hydrogen reduction at 673 or 823 K for 1 h was determined by static equilibrium adsorption of either $H_2$ at 373 K or CO at 298 K in a conventional vacuum system.

#### 2.2.3. X-ray diffraction (XRD)

The XRD patterns of the calcined solids and supports were obtained with an XD-D1 Shimadzu instrument, using Cu Kα radiation at 30 kV and 40 mA. The scan rate was 1.0°/min for values between $2\theta = 10^\circ$ and 70°.

#### 2.2.4. Temperature-programmed reduction (TPR)

An Ohkura TP-20022S instrument equipped with a TCD was used for the TPR experiments. To carry out a similar thermal treatment performed in the reaction system, the samples were heated up to 823 K in nitrogen flow, kept constant for 1 h and then cooled down in $N_2$ flow. Afterwards, they were reduced in a 5% $H_2$–Ar stream, with a heating rate of 10 K/min up to the maximum treatment temperature.

#### 2.2.5. Fourier transform infrared spectroscopy (FTIR)

The IR spectra were obtained using a Shimadzu FTIR 8101 M spectrometer with a spectral resolution of 4 $cm^{-1}$. The samples for the CO adsorption experiments were prepared by compressing the pure solids at 2 ton $cm^{-2}$ in order to obtain a self-supporting wafer (30 mg, 10 mm diameter). They were mounted in a transportable infrared cell with $CaF_2$ windows and external oven. The pre-treatment was performed in a high vacuum system. The samples were first reduced at 673 K during 1 h in flowing $H_2$ and then outgassed for 1 h at 673 K in a dynamic vacuum of $7 \times 10^{-4}$ Pa. After cooling to room temperature, a spectrum of the catalyst wafer was taken. After that, different CO pressures were admitted at 298 K into the cell, left in contact with the solid for 10 min, and then a spectrum was recorded. Spectra were also recorded after evacuation of the cell for 10 min at 298, 373, 473, 573 and 673 K.

#### 2.2.6. X-ray photoelectron spectroscopy (XPS)

The XPS measurements were carried out using a multi-technique system (SPECS) equipped with a dual Mg/Al X-ray source and a hemispherical PHOIBOS 150 analyzer operating in the fixed analyzer transmission (FAT) mode. The spectra were obtained with pass energy of 30 eV; an Mg Kα X-ray source was operated at 200 W and 12 kV. The working pressure in the analyzing chamber was less than $5.9 \times 10^{-7}$ Pa. The XPS analyses were performed on the supports and on the solids after treatment with hydrogen at 673 K carried out in the reaction chamber of the spectrometer. The spectral regions corresponding to La 3d, C 1s, O 1s, Si 2s, Ru 3d and Ru 3p core levels were recorded for each sample.

The data treatment was performed with the Casa XPS program (Casa Software Ltd., UK). The peak areas were determined by integration employing a Shirley-type background. Peaks were considered to be a mixture of Gaussian and Lorentzian functions in a 70/30 ratio. For the quantification of the elements, sensitivity factors provided by the manufacturer were used.

#### 2.2.7. Ion scattering spectroscopy (ISS)

The experiments were conducted in the same multi-technique system (SPECS). The He pressure in the analysis chamber was about $2 \times 10^{-5}$ Pa. The energy of the ion gun was 1.5 keV and the spectra were recorded at intervals of 5 min.

### 2.3. Catalytic test

#### 2.3.1. Fixed-bed reactor

The catalyst was loaded into a tubular quartz reactor (inner diameter, 5 mm) which was placed in an electric oven. The catalyst (10–30 mg) was diluted with 50 mg of inert powder quartz in order to avoid temperature gradients. A thermocouple in a quartz sleeve was placed on top of the catalyst bed. In this system, different treatments were carried out as follows:

(a) The catalysts were calcined at 823 K in air flow and then reduced in $H_2$ flowing at the same temperature.
(b) The uncalcined catalysts were heated up to 673 K in Ar flow, then reduced in flowing $H_2$, and after that heated from 673 to 823 K on stream.
(c) The uncalcined catalysts were heated up to 823 K in Ar flow and then reduced in $H_2$ flow at the same temperature.

After reduction, the reactant gas mixture ($P_{CO_2} : P_{CH_4} : P_{Ar} = 1 : 1 : 1.1$, $P = 1$ atm, $W/F = 4.5 \times 10^{-6}$ g h $ml^{-1}$) was fed to the

reactor. The reaction rate measurements under differential conditions were conducted in a conventional flow system. The reaction experiments were carried out at 823 K. The feed gases and the reaction products were analyzed in a thermal conductivity detector gas chromatograph (Shimadzu GC-8A) equipped with a Porapak column, and a molecular sieve column.

## 3. Results and discussion

### 3.1. Catalytic behavior

The activity and stability of Ru catalysts were measured in a conventional fixed-bed reactor. The results obtained after the different thermal treatments are summarized in Table 1. The $CO_2$ reaction rate was higher than the $CH_4$ reaction rate due to the simultaneous occurrence of the reverse water gas shift (RWGS) reaction in which $CO_2$ reacted with the $H_2$ produced in the reforming reaction; this is consistent with a $H_2/CO$ ratio lower than unity. The stoichiometry of these reactions leads to the following relationship: $H_2/CO = (3 - (r_{CO_2}/r_{CH_4}))/(1 + (r_{CO_2}/r_{CH_4}))$; where $r_{CH_4}$ and $r_{CO_2}$ are the experimental $CH_4$ and $CO_2$ reaction rates, respectively [4]. This equation was satisfied for all the measured points.

The calcined catalysts showed low reaction rate values and they deactivated after a few hours on stream (Table 1). Several possible causes for Ru-catalyst deactivation could be proposed, such as carbon deposition on the catalyst surface or increase of Ru particles size as well [16].

In the case of the uncalcined catalysts, two different treatments and reduction temperatures were employed. The stability tests for these catalysts are presented in Fig. 1a and b. All solids remained stable for more than 100 h in reaction. In addition, the reaction rates exhibited high values and were independent of the reduction temperature except for the case of $Ru/La_2O_3(40)–SiO_2$. This catalyst reduced at 823 K showed the lowest reaction rate while after reduction at 673 K it showed the highest value. It seems that the more severe treatment decreases the active sites dispersion on the solid, and this affects the catalytic activity for the $Ru/La_2O_3(40)–SiO_2$ solid.

Table 2 shows the turnover frequency values (TOF) of the uncalcined catalysts reduced at 673 and 823 K, as well as the Ru dispersion determined by CO chemisorption at room temperature, whereas the CO/Ru ratio was equal to 1. The Ru dispersions measured after reduction at 673 and 823 K were similar for each solid, except for $Ru/La_2O_3(40)–SiO_2$. This solid showed the greatest change in the reaction rate using different reduction temperatures. The lowest TOF was observed for the $Ru/La_2O_3(40)–SiO_2$ catalyst

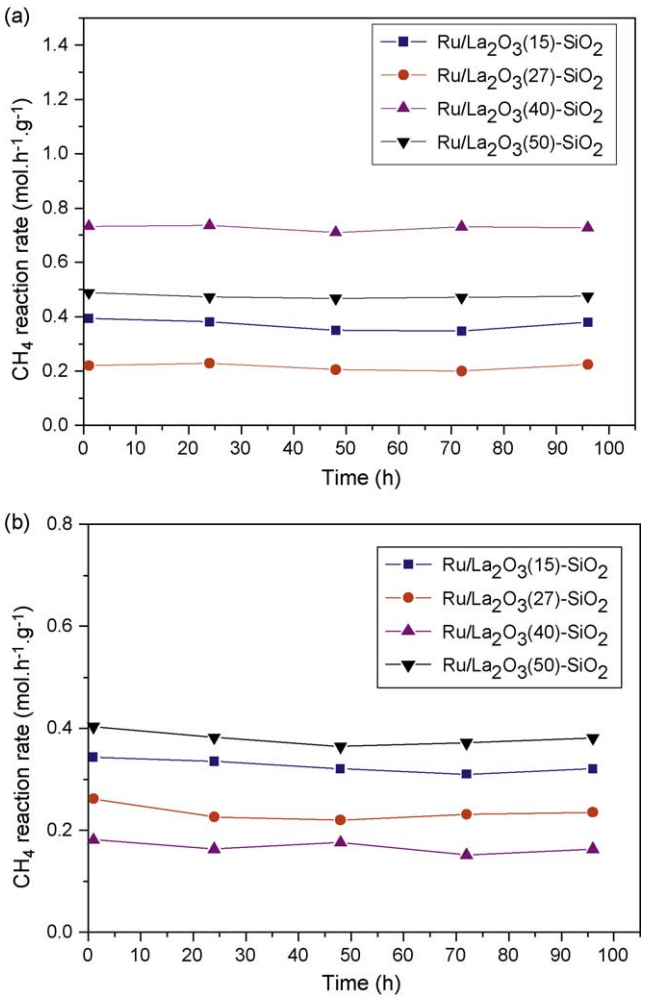


**Fig. 1.** (a) Stability test of the catalysts after reduction at 673 K in the fixed-bed reactor. (Reaction temperature = 673 K, W/F = $4.3 \times 10^{-6}$ g h $ml^{-1}$.) Feed composition: $P_{CH_4} : P_{CO_2} : P_{Ar} = 1 : 1 : 1.1$. (b) Stability test of the catalysts after reduction at 823 K in the fixed-bed reactor. (Reaction temperature = 823 K, W/F = $4.3 \times 10^{-6}$ g h $ml^{-1}$.) Feed composition: $P_{CH_4} : P_{CO_2} : P_{Ar} = 1 : 1 : 1.1$.

**Table 1**
$Ru/La_2O_3–SiO_2$ formulations. Catalytic activity after different treatments.

| Solids[a] | Treatments | $r_{CH_4}$ (mol $h^{-1}$ $g^{-1}$) | $r_{CO_2}$ (mol $h^{-1}$ $g^{-1}$) | $H_2/CO$ ratio |
|---|---|---|---|---|
| $Ru/La_2O_3(15)–SiO_2$ | $H_2$, 673 K, 2 h[b] | 0.39 | 0.82 | 0.30 |
| | $H_2$, 823 K, 2 h[c] | 0.34 | 0.73 | 0.27 |
| $Ru/La_2O_3(27)–SiO_2$ | Calcined, 823 K, 6 h[d] | 0.09[e] | 0.24 | – |
| | $H_2$, 673 K, 2 h[b] | 0.22 | 0.40 | 0.45 |
| | $H_2$, 823 K, 2 h[c] | 0.21 | 0.41 | 0.26 |
| $Ru/La_2O_3(40)–SiO_2$ | $H_2$, 673 K, 2 h[b] | 0.73 | 1.46 | 0.34 |
| | $H_2$, 823 K, 2 h[c] | 0.18 | 0.34 | 0.37 |
| $Ru/La_2O_3(50)–SiO_2$ | Calcined, 823 K, 6 h[d] | 0.05[f] | 0.08 | – |
| | $H_2$, 673 K, 2 h[b] | 0.49 | 0.87 | 0.48 |
| | $H_2$, 823 K, 2 h[c] | 0.40 | 0.68 | 0.36 |

[a] The wt.% of $La_2O_3$ is indicated between parentheses. All these solids contain 0.6 wt.% of Ru.
[b] The solids were heated up to 673 K in Ar flow, then were reduced in flowing $H_2$, and after that heated from 673 to 823 K on stream (gas mixture: $CH_4/CO_2/Ar$).
[c] The solids were heated up to 823 K in Ar flow, then were reduced in flowing $H_2$ at the same temperature.
[d] The calcined solids were reduced at 823 K.
[e] $r_{CH_4} = 0.06$ after 24 h on stream.
[f] $r_{CH_4} = 0.03$ after 24 h on stream.

**Table 2**
$La_2O_3$ content and reduction temperatures affect metal dispersion, TOF and surface area in $Ru/La_2O_3–SiO_2$ solids.

| Solids[a] | Treatments | $D_{CO}$[b] (%) | $TOF_{CH_4}$ ($s^{-1}$) | dp (nm) |
|---|---|---|---|---|
| $Ru/La_2O_3(15)–SiO_2$[c] | $H_2$, 673 K, 2 h[b] | 40 | 4.56 | 2.25 |
| | $H_2$, 823 K, 2 h[c] | 36 | 4.42 | 2.50 |
| $Ru/La_2O_3(27)–SiO_2$ | $H_2$, 673 K, 2 h[b] | 25 | 4.12 | 3.60 |
| | $H_2$, 823 K, 2 h[c] | 24 | 4.09 | 3.75 |
| $Ru/La_2O_3(40)–SiO_2$ | $H_2$, 673 K, 2 h[b] | 72 | 4.74 | 1.25 |
| | $H_2$, 823 K, 2 h[c] | 29 | 2.90 | 3.11 |
| $Ru/La_2O_3(50)–SiO_2$ | $H_2$, 673 K, 2 h[b] | 38[d] | 6.03 | 2.37 |
| | $H_2$, 823 K, 2 h[c] | 36 | 5.20 | 2.50 |

[a] The wt.% of $La_2O_3$ is indicated between parentheses.
[b] Dispersion measured from CO chemisorption.
[c] See footnotes b and c in Table 1.
[d] $D_{H_2} = 32\%$. Dispersion measured from $H_2$ chemisorption.

reduced at 823 K. This behavior could be related to the metal–support interaction. The low lanthanum content solids exhibit similar $TOF_{CH_4}$ values (TOF = 4.4 ± 0.3) independently of the reduction temperature. Note that the Ru/$La_2O_3$(50)–$SiO_2$ solid exhibits the highest $TOF_{CH_4}$ for both reduction treatments. Table 2 shows that there is no relationship between dispersion and TOF with the increase of the $La_2O_3$ load. Note that for all catalysts, the same Ru content was employed.

To calculate the Ru particle size, the following equation was applied

$$dp = \frac{6 \cdot \nu_m}{D \cdot a_m} \quad (1)$$

where $D$ is the metal dispersion (the ratio of the number of metal atoms on the support surface to the total number of metal atoms in the bulk), $\nu_m$ is the volume occupied by a metal atom (m) in the bulk, and $a_m$ is the surface area occupied by an exposed surface metal atom (m). Three parameters are then needed in order to calculate the average particle size. $\nu_m$ is $13.65 \times 10^{-3}$ nm$^3$ for Ru. The area occupied by a surface metal atom (m) on an exposed polycrystalline surface ($a_m$) is dependent on the nature of the crystal planes exposed on the metal surface. Ruthenium has a hexagonal close packed (hcp) unit cell structure. In previous studies, it has been shown that for Ru supported catalysts good results are achieved using an average surface area occupied by one Ru atom ($a_m$) (average from areas of (1 0 0), (0 0 1), and (1 1 0) planes). This value is $9.09 \times 10^{-2}$ nm$^2$ instead of $6.35 \times 10^{-2}$ nm$^2$ when assuming that only the (0 0 1) plane is exposed [17]. The metal dispersion, $D$, was calculated from CO chemisorption data (Table 2). Therefore, employing these $\nu_m$, $a_m$ values and the pertinent dispersion data, the volume–area mean diameter of Ru can be calculated from Eq. (1). These metal particle sizes are included in Table 2. Note that the average Ru particle sizes were independent of the reduction temperature except in the case of Ru/$La_2O_3$(40)–$SiO_2$.

Metal dispersion is a critically important parameter in catalytic behavior. The high dispersion of the metal on the composite support would be responsible for the high-reaction rates of these solids. Employing a similar $La_2O_3$(27)–$SiO_2$ binary support, we previously observed that the Rh TOF values decrease with increasing rhodium dispersion. The low TOF values suggest that the activity of the rhodium sites is lower than in the case of the Rh/$La_2O_3$ solids. Yokota et al. [18] studied the rhodium activity for different supports and concluded that Rh was structure sensitive in the $CO_2$–$CH_4$ reaction. The structure sensitivity was caused by the electronic interaction between Rh and the support surface [18]. The supports employed to disperse Ru crystallites [2–5] often influence the dry reforming rates, but concurrent effects of supports on Ru dispersion or a participation in the catalytic cycle are seldom independently considered. In this work, we studied the properties of the $La_2O_3$–$SiO_2$ binary supports and their influence in the nature of the Ru active sites.

### 3.2. Support characterization

The support surface area was measured after calcination at 823 K. The values were 188, 143, 88 and 53 m$^2$ g$^{-1}$ for the supports with 15, 27, 40 and 50 wt.% of $La_2O_3$, respectively. It was found that surface area decreases with increasing $La_2O_3$ loading.

Fig. 2 shows the diffractograms obtained for the silica and the binary supports calcined at 1173 K and 823 K, respectively. The diffraction patterns obtained for the $La_2O_3$–$SiO_2$ supports exhibit a shoulder at about $2\theta = 29^\circ$ and small broad reflections at $2\theta = 41^\circ$; these are symptomatic of the presence of lanthanum disilicate ($La_2Si_2O_7$) since these reflections coincide with the main peaks given for this compound (JCPDS No. 21-1014) [13,19]. As the $La_2O_3$ loading increases, it can be observed that the two broad peaks begin to grow in intensity. The lanthanum disilicate may impair the formation of oxycarbonate and hydroxide phases. The broadness of these peaks is characteristic of a phase with low crystallinity. In catalysts prepared by impregnating calcined silica with lanthanum nitrate, Vidal et al. [19] reported the formation of the same disilicate even for lower lanthanum loadings.

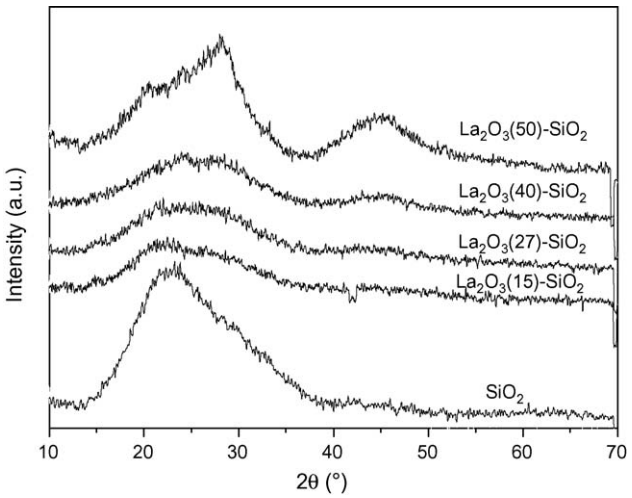


**Fig. 2.** XRD patterns for the silica and binary supports calcined at 1173 and 823 K, respectively.

The ISS technique is used to characterize supported systems providing information about the elemental composition of the outer layer, while XPS analyzes a depth of 30–40 Å. In our case, we studied the surface composition of the binary lanthanum silica supports employing both techniques. Fig. 3 shows ISS spectra for the supports with different percentages of lanthanum [20]. Three different peaks are observed, assigned to O, Si and La at 669.6, 954.6, and 1369.9 eV, respectively, when the $^4$He ion beam energy was 1500 eV. The intensity of the O peak at $E$ = 669.9 eV was normalized to show more clearly the change in the La and Si peak intensities for the different supports. Fig. 4 shows the La/Si surface ratio calculated from the ISS data. These were plotted as a function of the number of La atoms per nm$^2$ of support. It can be seen that the La/Si surface ratio increases with the lanthanum load; however, a significantly lower La/Si ratio was observed for the $La_2O_3$(50)–$SiO_2$ support. The maximum value was obtained for the $La_2O_3$(40)–$SiO_2$ solid.

The XPS surface atomic ratios were calculated with the integrated intensity of the La $3d_{5/2}$ and Si 2 s peaks. The Si 2p peak was not considered due to its overlapping with the La 4p peak. Note that the XPS La/Si ratio mimics the ISS La/Si ratio. These results could indicate that the coverage of lanthanum, probably forming a surface disilicate, increases up to 40 wt.% of $La_2O_3$ load and from there, the lanthanum oxide particle growth on the surface could occur.

The complex line shapes of the photoelectron spectra of rare-earth compounds have been shown to contain structural information. It is well known that these line shapes are due to hybridization effects between the valence band of the solid and localized f-states of the lanthanum ion in the final state of photoionization giving rise to the typical two-peaked shape of the La(3d) doublet components [21]. Hence, this shape will be observed in the presence of only one type of lanthanum species as it is due to the electronic structure in the final state of ionization. The intensity distribution between the maxima at high and low binding energies is related to the energy difference of the (uncoupled) $f^0$ and $f^1$ final states and the strength of

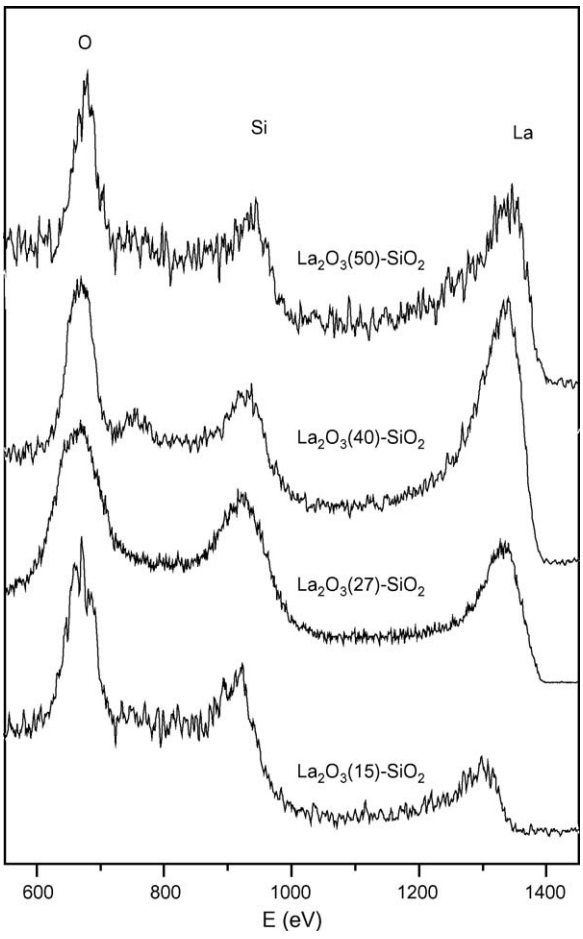


**Fig. 3.** ISS spectra for the calcined $La_2O_3$–$SiO_2$ binary supports.

hybridization. The former depends on the energy differences of the $f^0$ and $f^1$ initial states and may therefore reflect differences in the electronegativity and polarizability of the ligands contributing to the valence band.

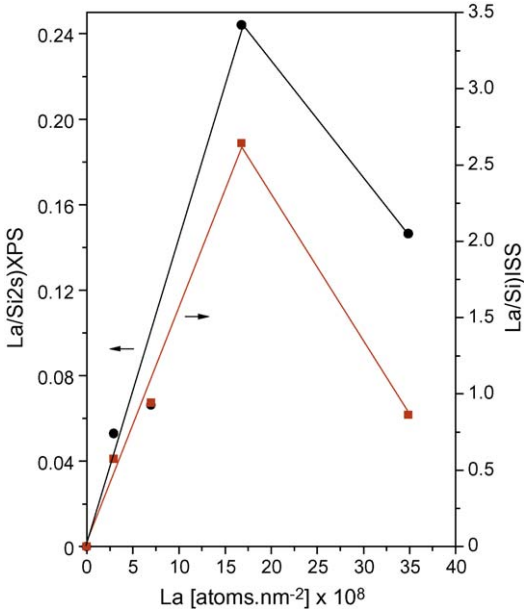


**Fig. 4.** La/Si surface ratios calculated by XPS and ISS data as a function of the La loading [atom $nm^{-2}$].

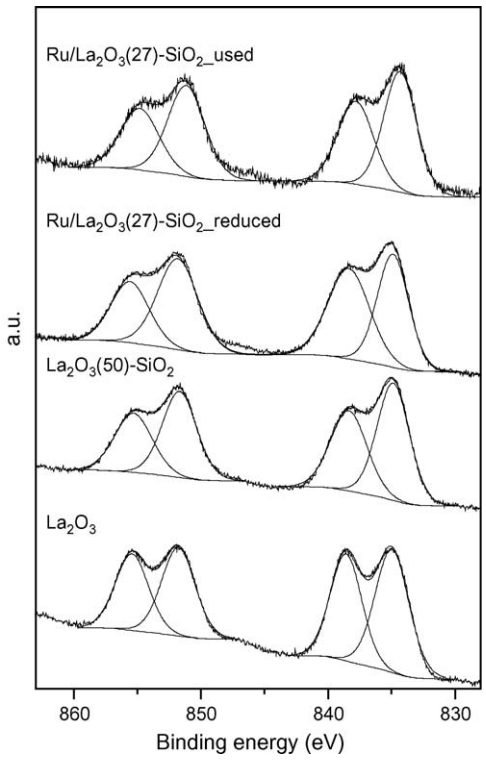


**Fig. 5.** La $3d_{5/2}$ XPS spectra from calcined $La_2O_3$, $La_2O_3$(50)–$SiO_2$ support, reduced $Ru/La_2O_3$(27)–$SiO_2$ and used $Ru/La_2O_3$(27)–$SiO_2$.

Fig. 5 shows the typical La $3d_{5/2}$ spectrum observed from the $La_2O_3$ sample calcined at 823 K. The XRD pattern shows the characteristic features of the $La_2O_2CO_3$ crystalline phase. The La 3d doublet is well defined showing the satellite structure appearing on the high side of $3d_{5/2}$ and $3d_{3/2}$ peaks. The La $3d_{5/2}$ core level is observed at 834.9 eV and the corresponding satellite split is 3.6 eV. These values agree well with those previously reported for the $La_2O_3$ blank by Gallaher et al. [22]. In our case, the satellite/main peak ratio is close to 0.81, while the peak shows a full width at half maximum (FWHM) close to 3.1 eV. Besides, Fig. 5 compares the La 3d spectra for different $La_2O_3$–$SiO_2$ samples. The main features of the La 3d peaks are summarized in Table 3. The binding energy values are close to 834.8 ± 0.2 eV. All samples exhibit a broad La $3d_{5/2}$ satellite (FWHM larger than 3.2 eV). Besides, the satellite/main peak intensity ratio is generally higher than the value observed in the lanthanum oxide sample calcined at 823 K, with the exception of the $La_2O_3$(50)–$SiO_2$ support which presents a value close to 0.76.

Karge and coworkers [21] studied the effect of the zeolite matrix on the La(3d) binding energy and line shape for La-exchanged zeolite samples. The authors compared the La signal

**Table 3**
XPS binding energies (eV) for La 3d regions.

| Samples | La $3d_{5/2}$[a] | La satellite[a] | Isat/IMP[b] | ΔMP-Sat[c] |
|---|---|---|---|---|
| $La_2O_3$ | 834.9(3.1) | 838.6(2.9) | 0.81 | 3.7 |
| $La_2O_3$(50)–$SiO_2$ | 834.9(3.0) | 838.4(3.3) | 0.76 | 3.5 |
| $Ru/La_2O_3$(15)–$SiO_2$ | 834.6(2.8) | 838.1(3.8) | 1.10 | 3.5 |
| $Ru/La_2O_3$(27)–$SiO_2$ | 834.9(2.9) | 838.4(3.9) | 1.05 | 3.5 |
| $Ru/La_2O_3$(40)–$SiO_2$ | 834.6(2.9) | 838.1(3.5) | 0.91 | 3.5 |
| $Ru/La_2O_3$(50)–$SiO_2$ | 834.6(2.8) | 838.1(3.3) | 0.94 | 3.5 |

For all samples, the binding energies of C and Si were the following: C 1s = 284.8 eV, Si 2s = 153.5 ± 0.1 eV.
[a] FWHM (eV) are shown between parenthesis.
[b] Satellite/main peak intensity ratio for La $3d_{5/2}$.
[c] Main peak – satellite splits for La $3d_{5/2}$.

shapes between $La_2O_3$ and the La zeolites, and attributed the decreased contribution of the high-BE La component in the zeolites to the fact that the La ions are coordinated by $H_2O$ molecules and by oxygen engaged in the partially covalent bonding of the zeolite framework. In this environment, where less charge is supplied by the less polarizable ligands for the screening of the photoelectron hole, the $f^1$ final state shifts to higher energies, which impairs the hybridization with the $f^0$ final state. The consequence is a decreased contribution of the high-binding energy (BE) satellite and a smaller separation between the maxima.

In the same way, Makshina et al. [23] studied bulk lanthanum cobaltate ($LaCoO_3$) with perovskite-like structure and $LaCoO_x$ supported onto the mesoporous molecular sieve through XPS. The appearance of a satellite peak on the La $3d_{5/2}$ peak was observed in both types of samples. The difference in the satellite and main La 3d peak intensity ratio between $LaCoO_3$ and MCM-41-supported $LaCoO_x$ confirmed that the lanthanum was present in an environment different from $LaCoO_3$.

A similar effect could be present in the binary $La_2O_3$–$SiO_2$ supports where we can observe (Table 3) a higher intensity of the high-BE satellite compared to the one in the pure lanthanum solid. Note that Si has a lower electronegativity and is a more polarizable ligand. This behavior is in agreement with the possible formation of a well-dispersed lanthanum disilicate phase on the support surface.

For binary $La_2O_3$–$SiO_2$ supports, Vidal et al. [19] proposed a full coverage of the silica surface with a disilicate phase based upon the data obtained from both the hydration and carbonation of samples with different $La_2O_3$ loads.

### 3.3. Catalyst characterization

#### 3.3.1. Calcined catalysts

Fig. 6 shows the diffractograms of the calcined catalysts with different $La_2O_3$ loading and for the $Ru/Al_2O_3$ solid prepared for comparison. The latter solid has peaks at $2\theta = 28.5$, 34.8 and 55° assigned to $RuO_2$ species [24]. In the calcined solids, these peaks are present with lower intensity, indicating the formation of ruthenium oxide crystals. For these samples, after $H_2$ reduction at 823 K and the dry reforming reaction, the diffractograms show very low-intensity metallic Ru signals indicating the presence of a crystalline phase (not shown). These reflections were used to calculate the average crystallite size (d) using the Scherrer equation,

$$\mathrm{dp} = \frac{k \cdot \lambda}{\beta \cdot \cos\theta} \quad (2)$$

where $\lambda$ is the wavelength of X-ray sources (for Cu Kα, $\lambda = 1.5406$ Å), $\beta$ is the angular width of the peak, $\theta$ is half of the diffraction angle and $k$ is the shape factor of the average crystallite.

Crystallite size is the major source leading to line broadening effects of diffraction peaks, but crystal strain and the XRD instrument itself can also introduce peak broadening. So, the angular width of the peak can be expressed by,

$$\beta = \sqrt{(FWHM)^2 - b^2} \quad (3)$$

where $b$ is the instrumental broadening. For this calculation, the instrumental line broadening ($b$) was negligible. Then, we considered that $\beta \approx FWHM$. This approach is supported by data from the literature [17].

The calculated particle sizes were around 20–30 nm for all the used catalysts. As discussed above, these catalysts deactivated after a few hours on stream. Furthermore, we also said before that several possible causes for Ru-catalyst deactivation could be proposed, such as carbon deposition on the catalyst surface or increase of Ru particles size as well [16]. Note that no carbon formation was observed by Laser Raman spectroscopy. This result and the values of calculated particle sizes suggest that the deactivation of the calcined solids could be due to the sintering of the active phase.

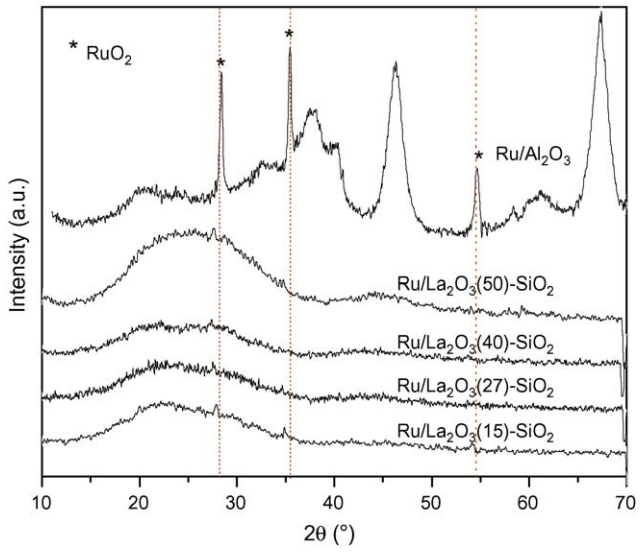


**Fig. 6.** XRD patterns for the $Ru/La_2O_3$–$SiO_2$ and $Ru/Al_2O_3$ catalysts (prepared for comparison).

### 3.4. Uncalcined catalysts

No XRD reflections associated with Ru species were detected in the uncalcined catalysts after the reduction treatments.

These solids were characterized employing several techniques trying to unravel the nature of the differences in the active sites that confer a high stability.

#### 3.4.1. Reducibility of Ru species

The reducibility of the supported ruthenium catalysts was studied by temperature-programmed reduction. To carry out a thermal treatment similar to that performed in the reaction system, the samples were heated up to 823 K in nitrogen flow, kept constant for 1 h and then cooled down in $N_2$ flow. The $Ru/SiO_2$ and $Ru/La_2O_3$ were included for comparison. The TPR profiles of the $Ru/La_2O_3$–$SiO_2$ catalysts showed two main reduction peaks (Fig. 7). The reduction temperature increased with the La loading except for $Ru/La_2O_3(40)$–$SiO_2$.

Yan et al. [24] reported two reduction peaks at 423 and 473 K in $Ru/SiO_2$ catalysts. The low temperature peak has been assigned to well-dispersed $RuO_x$ species and the high temperature peak has been attributed to $RuO_2$ particles [7]. Vidal et al. [25] studied the reducibility of the uncalcined $Rh/La_2O_3$–$SiO_2$ catalyst and assigned the reduction peak at 450 K to the reduction of species generated in the lanthana redissolution process. This peak was lower for the support calcined at high temperature. Bernal et al. [26] suggested that the impregnation of the $La_2O_3$–$SiO_2$ system, previously calcined at 873 K with an aqueous solution of Rh nitrate, induces the leaching of the lanthanum containing phase. They sustained that calcination at 1173 K would prevent the leaching of the phase maybe due to the formation of $La_2Si_2O_7$.

In previous studies of $Ru/La_2O_3$ solids, laser Raman spectroscopy and TPR indicated the presence of Ru(III) strongly interacting with lanthanum [10]. The hydrogen consumption was calculated for our solids supported on $La_2O_3$–$SiO_2$. For all catalysts, the μmol $H_2$/μmol Ru ratio was about 1.4–1.5, lower than the ratio

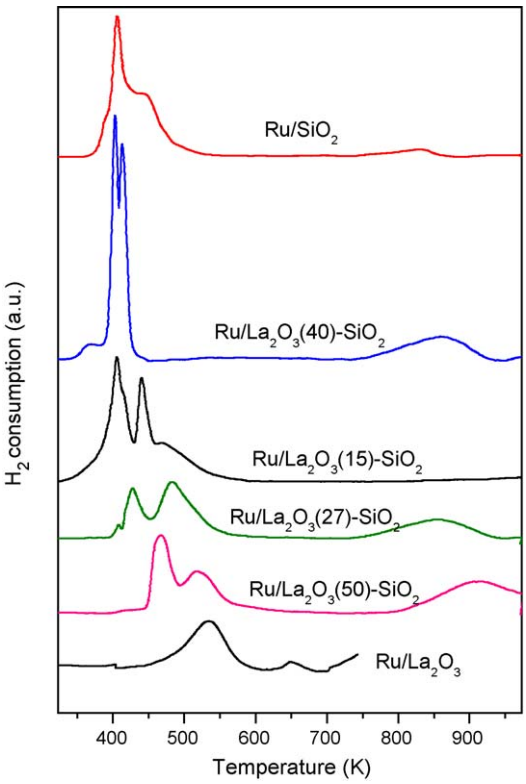


**Fig. 7.** TPR profiles of Ru catalysts treated in $N_2$ flow at 823 K in the TPR system.

expected for $RuO_2$. These results suggest the presence of Ru(III) species. In $Ru/La_2O_3(50)–SiO_2$, the reduction peaks appear at higher temperature. This is symptomatic of a stronger metal–support interaction, in agreement with the possible particle growth of $La_2O_3$ oxide observed through XPS and ISS. In fact, the small high temperature peak above 750 K may be related to the decomposition of lanthanum oxycarbonate. The released $CO_2$ detected in the TPR profile of the Ru catalyst corresponds to 1% of the total $La_2O_3$ present, suggesting that the availability of $La_2O_3$ to form the oxycarbonates is limited.

### 3.4.2. CO adsorption

The characteristics of the Ru surface species were investigated by CO adsorption FTIR. CO is one of the most used probe molecules, revealing the oxidation and the coordination state of the sites to which it is bound. There are many works dealing with CO adsorption on supported ruthenium catalysts. The results obtained are more complicated than those observed with other noble metals and the formation of different kinds of carbonyls has been proposed. In general, the CO bands arising from CO adsorption on supported ruthenium catalysts are divided into three groups: $HF_1$ (high-frequency 1) at 2156–2133 $cm^{-1}$, $HF_2$ at 2100–2060 $cm^{-1}$ and LF (low frequency) bands at about 2060–1970 $cm^{-1}$ (Table 4) [27–31]. The literature data allowed us to distinguish at least three different kinds of species associated with the above bands.

Type I carbonyls were identified through CO adsorption on ruthenium single crystals [32,33] which showed that the linear $Ru^0$–CO carbonyls are characterized by an LF band at about 2040 $cm^{-1}$. The position of this band strongly depends on the coverage and on the metal–support interaction and is usually more intense than the bands of the other two groups, $HF_1$ and $HF_2$. However, the absorption frequency is not a sufficiently reliable criterion for the identification of $Ru^0$–CO carbonyls because vibrations of ionic carbonyls may also be observed in the same region (type III carbonyls) [28].

**Table 4**
Vibration frequencies of a linear, bridge and of monocarbonyls and $Ru^{n+}(CO)_x$ carbonyls adsorption (gem) ($\nu_l$, $\nu_b$, $\nu_m$ and $\nu_g$, respectively).

| | This work | Wavenumber | References |
|---|---|---|---|
| $\nu_l$ ($cm^{-1}$) | 2049 | 2060–1970 | [27] |
| $\nu_b$ ($cm^{-1}$) | 1942 | 1920–1955 | [29] |
| $\nu_m$ ($cm^{-1}$) | 1980 | 1900–2000 | [29] |
| $\nu_g$ ($cm^{-1}$) | $HF_1/HF_2$: 2144/2074<br>$HF_2$/LF: 2084/2014 | $HF_1/HF_2$: 2156–2133/ 2100–2060<br>$HF_2$/LF: 2100–2060/ 2060–1970 | [31] |

Type II carbonyls are characterized by the $HF_1$–$HF_2$ set of bands. The interpretations of the $HF_1$ and $HF_2$ bands are quite contradictory. It has been established that (i) these two bands characterize ionic carbonyls, (ii) the $HF_1/HF_2$ intensity ratio is equal to 0.54, and (iii) the $HF_1$ bands and at least a fraction of the $HF_2$ bands represent vibrations of $Ru^{n+}(CO)_x$ multicarbonyls. The frequencies of the $HF_1$ and $HF_2$ bands are independent of the coverage [28].

Type III carbonyls are characterized by the $HF_2$-LF set of bands. Irrespective of the parallel intensity changes of the HF bands during adsorption, the $HF_1/HF_2$ intensity ratio decreases after desorption at elevated temperatures (intensity ratio of ca 0.54). This indicates that the $HF_2$ band is complex and part of it is due not only to type II carbonyls but also to another type of compounds (type III). Main data from the literature point out that the species under consideration are $Ru^{n+}(CO)_2$ dicarbonyls, where the oxidation state of ruthenium differs from its oxidation state in type II carbonyls. These compounds are characterized by a pair of bands at 2092–2045 ($HF_2$) and 2038–1970 $cm^{-1}$ (LF) [28].

Fig. 8 shows the spectra of the reduced $Ru/La_2O_3–SiO_2$ solids exposed at $1.3 \times 10^3$ Pa of CO. They present bands at about 2049 $cm^{-1}$ as the result of linearly adsorbed CO on metallic Ru ($Ru^0$–CO), bands typical of $Ru^{n+}(CO)_x$ carbonyls (2144, 2084, 2074 and 2014 $cm^{-1}$) and the bridged-bonded CO at about 1942 $cm^{-1}$ (Table 4). The broadening at 1950–2000 $cm^{-1}$ may be attributed to monocarbonyl species adsorbed on oxidized Ru sites. The signal is clearly resolved during thermal desorption at 473 K, where its maximum turns out to be located at 1980 $cm^{-1}$. Gupta et al. [30] assigned this band to monocarbonyl species on oxidized sites. They have been reported to arise from the desorption of CO from the multicarbonyl species responsible for the IR band above 2074 $cm^{-1}$, which seems to be the case also in the present experiments. Although the band at 1980 $cm^{-1}$ may already exist at room temperature, it grows in intensity with increasing temperature, probably at the expense of the 2144 $cm^{-1}$ band. This linearly bonded CO on $Ru^+$ ions may result from the oxidative disruption of small $Ru^0$ metal clusters [31]. Curve fittings were made for the spectra of the catalysts with different contents of lanthanum. Only slight differences were observed in the proportion of the CO adsorbed species.

All the bands described above are also present in $Ru/SiO_2$. However, the $Ru^0$–CO band appears at 2025 $cm^{-1}$. The band shift observed in the Ru–La based catalysts could be partially caused by a less significant dipole–dipole coupling between neighbouring CO molecules, in view of a larger separation between adsorbates on these catalysts, related to the high Ru dispersion observed.

Hadjiivanov et al. [27] reported that the $HF_1$ and $HF_2$ bands also appear after CO adsorption on completely reduced samples. In this case, the more significant peculiarities are the following: (i) a higher dispersion of the supported metal results in more intense bands; (ii) heating under CO at even higher temperatures leads to a decrease in intensity or disappearance of the bands.

The higher type II to type I carbonyls intensity ratio (Fig. 8) observed for all $Ru/La_2O_3–SiO_2$ solids supports the above finding

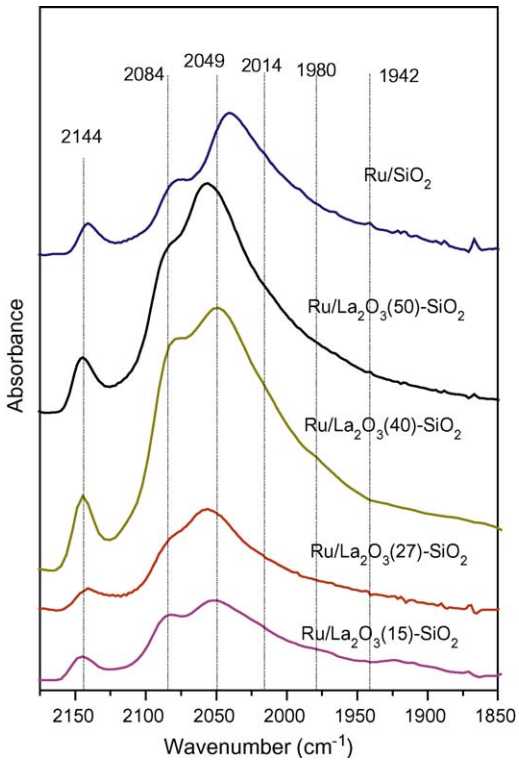


**Fig. 8.** FTIR spectra obtained from Ru catalysts reduced in hydrogen at 673 K after exposure to CO at 298 K ($P_{CO}$ = 1.3 × $10^3$ Pa).

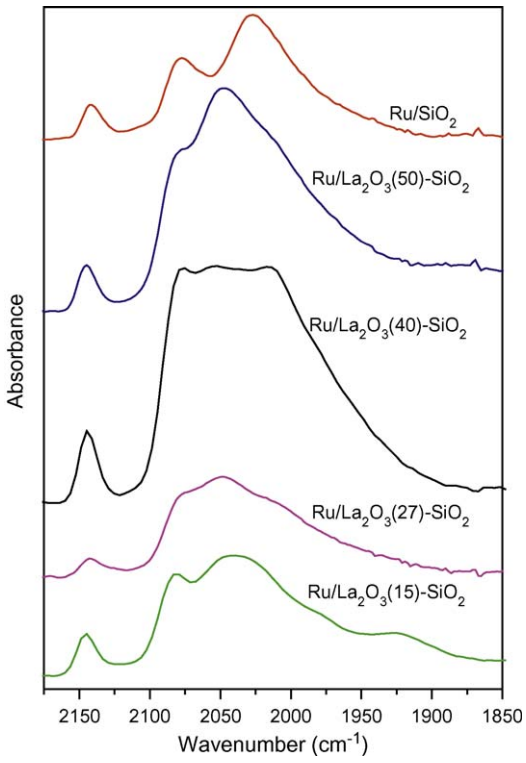


**Fig. 9.** FTIR spectra obtained from Ru catalysts reduced in hydrogen at 673 K, following CO adsorption and after desorption in dynamic vacuum at 298 K.

concerning the high Ru dispersion of $La_2O_3$–$SiO_2$ supported catalysts as compared to that of Ru/$SiO_2$ ($D_{CO}$ = 4%).

Fig. 9 shows the spectra after evacuating the cell at 298 K. The 2049 $cm^{-1}$ signal decreases while the other bands remain constant for all the catalysts. The decrease in the $Ru^0$–CO signal is more significant for Ru/$La_2O_3$(40)–$SiO_2$ compared to the other binary supports.

To show the differences in the CO adsorbed species, the curve fitting of the CO spectra after evacuation at 298 K was performed. The results obtained for Ru/$La_2O_3$(40)–$SiO_2$ and Ru/$La_2O_3$(50)–$SiO_2$ are shown in Fig. 10. The contribution of all the CO adsorption states was considered and their integrated intensities were measured. The linear $Ru^0$–CO signal to type II carbonyls intensity ratio is lower for Ru/$La_2O_3$(40)–$SiO_2$. This fact suggests that the carbonyl groups have a moderate stability in agreement with the $TOF_{CH_4}$ values (Table 2) and the lower metal–support interaction observed by TPR.

The thermal stability of the CO species adsorbed on the reduced Ru/$La_2O_3$–$SiO_2$ and Ru/$SiO_2$ catalysts was studied (Fig. 11a–c). The spectra obtained for Ru/$La_2O_3$(40)–$SiO_2$ after CO adsorption at 298 K at two different pressures and the subsequent stepwise heating under a dynamic vacuum to 673 K are shown in Fig. 11a. The signals assigned to $Ru^{n+}$(CO) and bridged-bonded CO species were more discernible at higher coverage (trace b). When the CO pressure increased, no band shifts were detected (traces a and b).

With increasing temperature, the band located at 2144 $cm^{-1}$ decreases without exhibiting any frequency shift and disappears above 473 K (trace e). At the same time, the linear $Ru^0$–CO signal progressively shifts to higher frequency with increasing temperature (from 2049 $cm^{-1}$ at 298 K to 2065 $cm^{-1}$ at 573 K). Besides, this band has a considerable decrease during thermal desorption (traces d–f) and type III carbonyls become clearly resolved. The 1980 $cm^{-1}$ band is very stable and could be more clearly visible in traces e and f. All bands disappear above 673 K (trace g).

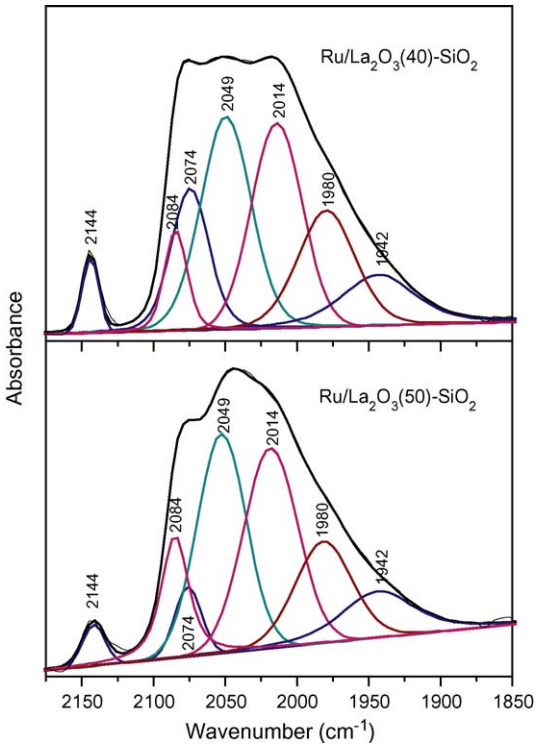


**Fig. 10.** FTIR spectra fit obtained from Ru catalysts reduced in hydrogen at 673 K, following CO adsorption and after desorption in dynamic vacuum at 298 K.

The spectra obtained with Ru/$La_2O_3$(50)–$SiO_2$ after the same adsorption and desorption steps showed similar changes (Fig. 11b). The main difference is between traces c which were previously assigned to the different Ru–La interaction observed in these solids (Fig. 10). However, the spectra measured for the Ru/

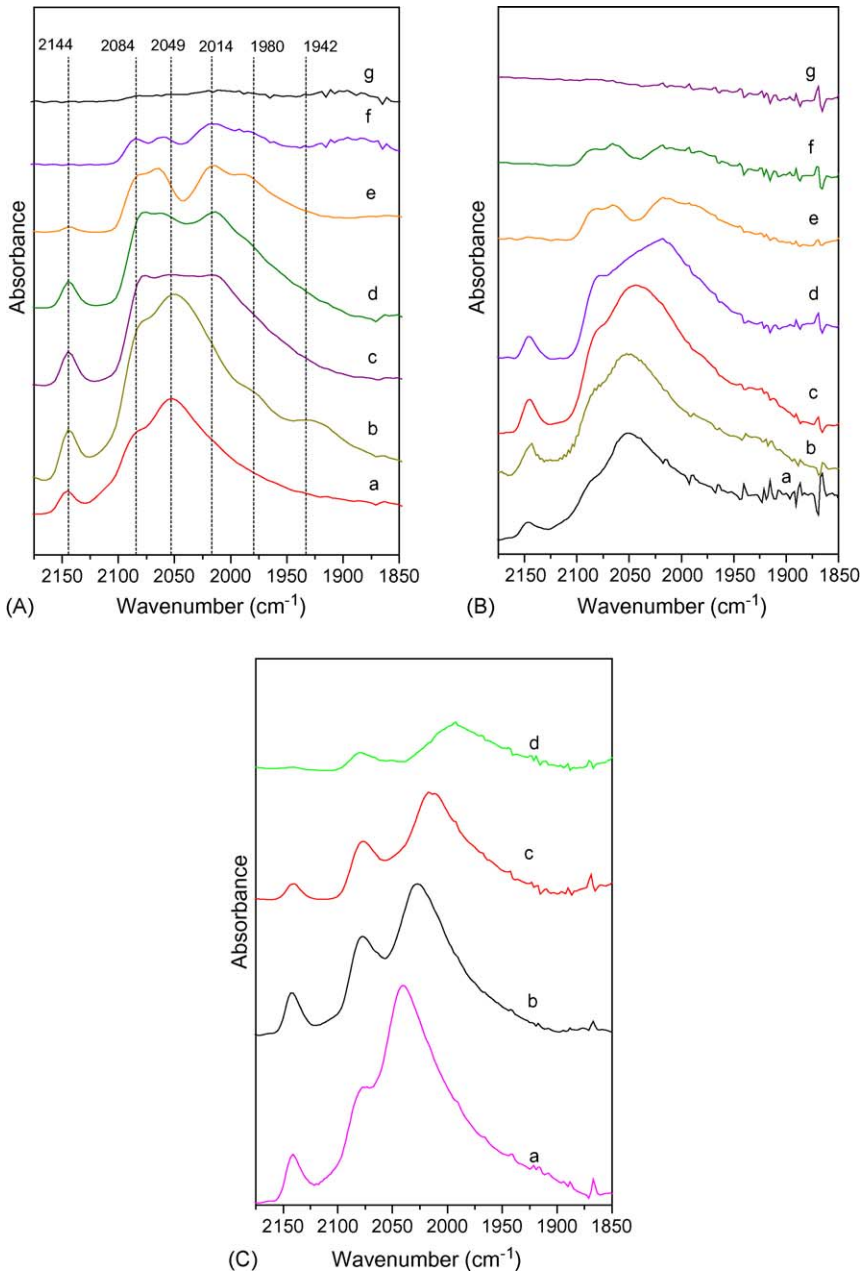


**Fig. 11.** (A) FTIR spectra obtained from $Ru/La_2O_3(40)–SiO_2$ reduced in hydrogen at 673 K following CO adsorption at 298 K, $P_{CO}$ = 6.6 Pa (a) and $P_{CO} = 6.6 \times 10^3$ Pa (b) and after stepwise heating under a dynamic vacuum to 298 K (c), 373 K (d), 473 K (e), 573 K (f) and 673 K (g). (B) FTIR spectra obtained from $Ru/La_2O_3(50)–SiO_2$ reduced in hydrogen at 673 K following CO adsorption at 298 K, $P_{CO}$ = 6.6 Pa (a) and $P_{CO} = 6.6 \times 10^3$ Pa (b) and after stepwise heating under a dynamic vacuum to 298 K (c), 373 K (d), 473 K (e), 573 K (f) and 673 K (g). (C) FTIR spectra obtained from $Ru/SiO_2$ reduced in hydrogen at 673 K following CO adsorption at 298 K, $P_{CO} = 6.6 \times 10^3$ Pa (a) and after stepwise heating under a dynamic vacuum to 298 K (b), 373 K (c) and 473 K (d).

$SiO_2$ catalyst exhibit a different behavior when the temperature is increased (Fig. 11c).

After evacuating the cell at 298 K, the linear $Ru^0$–CO signal decreases considerably and shifts to a higher wavenumber. This trend is enhanced when the temperature is increased and disappears at about 473 K. With increasing temperature, the intensity of the band located at 2144 $cm^{-1}$ decreases without exhibiting any frequency shift and disappears above 473 K (trace d). However, the band at 2084 $cm^{-1}$ is present at this temperature and can be assigned to the $HF_2$ band from the carbonyl type III species. The 1980 $cm^{-1}$ band is stable at temperatures above 473 K and the bridged-bonded CO species disappear at about 373 K.

The differences in the adsorbed CO species stability between Ru supported on silica or on binary $La_2O_3$–$SiO_2$ supports could be assigned to the presence of lanthanum, forming an incipient $La_2Si_2O_7$ phase that influences the metal–support interaction and metal dispersion.

### 3.4.3. Surface characterization

Fig. 12 shows the Ru 3d XPS spectra obtained on the reduced catalysts. Binding energies were referenced to C 1s = 284.8 eV, which resulted in a B.E. for La $3d_{5/2}$ = 834.4 ± 0.2 eV for all the ruthenium solids. There is an overlap between Ru 3d and C 1s peaks at 284.8 eV, the latter being due to carbonaceous contamination.

The C 1s spectra also exhibit a peak at 287.8 eV that was attributed to carbonaceous species associated with oxygen and/or hydrogen. The Ru peak appears at 280.1 eV. The O 1s spectra show two peaks: one at 531.2 eV assigned to the C–O and/or Si–O

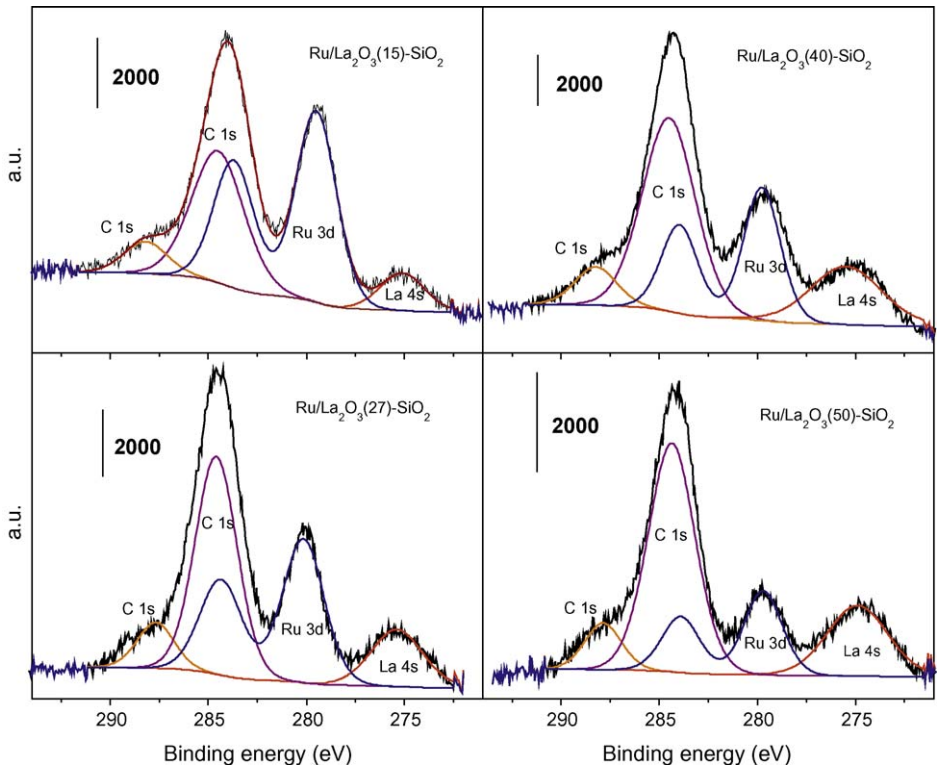


**Fig. 12.** Ru 3d XPS spectra from $Ru/La_2O_3–SiO_2$ reduced at 673 K in situ.

species and another at 528.8 eV corresponding to lattice oxygen $O^{2-}$ [34].

The Ru state with a BE of 282 eV is known from the literature and has been assigned [31] to Ru(IV)/Ru(III) oxyhydrates, $Ru^{2+}$ on $Al_2O_3$, and $Ru^{+}$ in Y zeolite. Elmasides et al. [31] assigned this BE to an intermediate Ru oxidation state, most likely Ru(II). This state appeared to be stable on $Al_2O_3$. They [31] found that on alumina, ruthenium is incompletely reduced by treatment with $H_2$ at 823 K while on $TiO_2$, Ru is more easily reduced to the metallic state. They found that the chemical behavior strongly depends on the material on which it is supported.

For the mixed $LaRu_{1-x}Ni_xO_3$ perovskite-type oxides, two well-defined peaks of Ru $3d_{5/2}$, one at ≈280 eV attributed to $Ru^0$ and a second one at ≈282.6 eV corresponding to unreduced Ru (Ru(III)) were reported by Goldwaser et al. [35]. In calcined $Ru/La_2O_3$ solids, we previously assigned the 282 eV peak to Ru(III) species [10]. After reduction, there appeared a peak at 280.2 eV that corresponds to $Ru^0$. The peak at 281.8 eV was still present but in low proportions. The complete surface reduction to $Ru^0$ was observed by XPS for all $Ru/La_2O_3–SiO_2$ catalysts. This fact suggested that $Ru^{n+}$(CO) monocarbonyls species were formed over re-oxidized Ru during the exposure to CO at low pressure. The XPS intensity ratios are given in Table 5. Comparing the Ru/La ratios, the Ru metallic surface content decreases with the increase in the lanthanum loading, while the Ru/La + Si ratio does not present a clear trend.

**Table 5**
Surface atomic ratio of $Ru/La_2O_3–SiO_2$ reduced at 673 K.

| Solids | Ru/La $3d_{5/2}$ | Ru/(La + Si 2s) |
|---|---|---|
| $Ru/La_2O_3(15)–SiO_2$ | 0.175 | 0.0088 |
| $Ru/La_2O_3(27)–SiO_2$ | 0.075 | 0.0065 |
| $Ru/La_2O_3(40)–SiO_2$ | 0.049 | 0.0097 |
| $Ru/La_2O_3(50)–SiO_2$ | 0.040 | 0.0038 |

### 3.5. Proposed model for Ru supported on binary $La_2O_3–SiO_2$ solids

Based on the results and the above discussion, we propose a model for the $Ru/La_2O_3–SiO_2$ catalysts. It takes into account two key factors: (i) the formation of a surface layer of lanthanum disilicate and (ii) the influence of lanthanum upon the Ru particle size and the metal–support interaction (Fig. 13).

The XPS and ISS results indicated that the full coverage by a lanthanum disilicate layer occurred at 40 wt.% of $La_2O_3$. At low La loadings, the Ru particle size was between 2 and 3 nm. However, when the full coverage by the disilicate was observed, the particle size was 1 nm, in agreement with the low reduction temperature (TPR) and the mild stability of the $Ru^0$–CO adsorbed species (FTIR). Then, metallic Ru was present in a highly dispersed state as fine particles (Fig. 13b). For this solid, when the reduction temperature increased to 823 K, the Ru

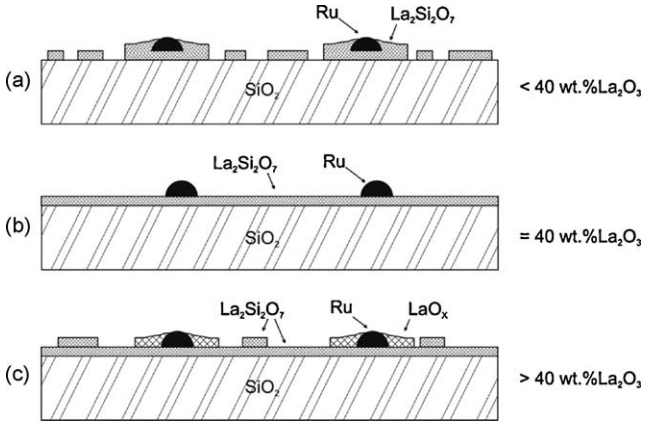


**Fig. 13.** Proposed scheme for $Ru/La_2O_3–SiO_2$ catalysts; (a) $Ru/La_2O_3(x)–SiO_2$, with $x < 40$ wt.% (b) $Ru/La_2O_3(40)–SiO_2$ and (c) $Ru/La_2O_3(50)–SiO_2$.

dispersion decreased suggesting metal particle sintering in agreement with the lower Ru–La interaction.

When the support contained 50 wt.% of $La_2O_3$, $LaO_x$ particles appeared and a strong Ru–La interaction was observed by both XPS and TPR. On the basis of these results, we can speculate that the LaOx formed after the catalyst reduction partially covered the Ru particle leading to a decrease in the CO chemisorption (Fig. 13c). This catalyst showed the highest TOF suggesting that more reactive particles are present when a strong Ru–La interaction is observed.

Wei and Iglesia [5,36] also showed that the turnover frequency increases with increasing dispersion, indicating that the detailed metal nanoparticle structure plays a role in it. Furthermore, Harrison and coworkers [37] reported that $CH_4$ thermal dissociative sticking coefficients on Ru(0 0 0 1) surfaces were as much as 3–4 orders of magnitude higher than the apparent sticking coefficients derived from $CH_4$ decomposition or reforming rates on supported nanoscale metal catalysts. They also emphasized that several surface science studies on single crystals strongly suggested that relatively few surface sites were turning over on the $CH_4$-reforming nanocatalysts.

When Ru and other noble metals are supported on non-carbonate forming oxides such as $Al_2O_3$ or $SiO_2$, Iglesia and coworkers [5,36] showed that the reaction kinetics are first-order in methane and zero order in $CO_2$ partial pressures. However, for $Ni/La_2O_3$ and $Rh/La_2O_3$ catalysts, the $CO_2$ reaction order varies between 0.37 and 0.50. This is symptomatic of the strong interaction between $CO_2$ and $La_2O_3$ which is reflected in the formation of oxycarbonates at the surface and the bulk level, at least after being exposed to the reacting mixture. In the case of $Rh/La_2O_3(27)–SiO_2$, the proportion of oxycarbonate formed was much lower mainly due to the presence of lanthanum disilicate which restricts the amount of $La_2O_3$ available to react with $CO_2$.

For these lanthanum based catalysts, the mechanistic picture previously proposed is that methane reversibly adsorbs on the metallic clusters while the cracking of the adsorbed species proceeds slowly liberating $H_2$ and generating carbon that remains on the metallic surface. The $CO_2$ rapidly reacts with $La_2O_3$ to generate oxycarbonate which in turn reacts slowly with carbon to generate the other main product, CO. This slow reaction most likely occurs at the metal/support interface.

When rich $CO_2$ streams were employed, we found that partial re-oxidation of metallic Ru could be one of the factors that produces the $Ru/La_2O_3$ deactivation. This effect could be more pronounced at $T > 873$ K [38]. Matsui et al. [9] studied the effect of support on the activities and mechanisms in the $CO_2$ reforming of methane over $Ru/La_2O_3$ catalysts. They proposed the following reaction step based on $CO_2$ pulse experiments

$$Ru/La_2O_3 + CO_2(ad) \Rightarrow CO(gas) + Ru{-}Ox/La_2O_3$$

In the literature, different studies invoke various parameters to be included in the kinetic expression in order to readily explain other phenomena, such as pressure dependency [39]. Therefore, it might be the case that the activity is not governed by a single rate determining step, but different rate determining steps depending on the reaction conditions [40,41]. Jones et al. [40] built up a complete picture of the reactivity of pure metal catalysts for steam reforming using recently identified scaling relationships in combination with thermodynamic and kinetic models. Theoretically, they observed that at low temperatures and for the noble metals the CO formation step is kinetically the most important reaction step. However, as the temperature and reactivity of the metal increase, i.e. the metal becomes less noble, the most kinetically relevant step switches from being CO formation to dissociative methane adsorption. They sustained that this is a possible explanation for the fact that several studies, carried out under different conditions, find different rate determining steps.

## 4. Conclusions

The activity and stability of Ru catalysts after different treatments were measured in a conventional fixed-bed reactor for the dry reforming of methane.

The calcined solids showed low reaction rate values and they deactivated after few hours on stream. The deactivation could be due to the sintering of the active phase observed by XRD.

The uncalcined solids remained stable for more than 100 h on stream. They exhibit high-reaction rate values and were independent of the reduction temperature except for the case of $Ru/La_2O_3(40)–SiO_2$.

The $TOF_{CH_4}$ values present a minimum for the $Ru/La_2O_3(40)–SiO_2$ solid, in agreement with a lower metal–support interaction. The $Ru/La_2O_3(50)–SiO_2$ catalyst exhibits the highest $TOF_{CH_4}$ for both reduction treatments.

By means of XPS and ISS, we obtained information about the distribution of lanthanum in the support. The formation of a surface $La_2Si_2O_7$ phase was suggested for samples containing $La_2O_3$ up to 40 wt.%. Higher contents could lead to a $La_2O_3$ particle growth. This could be the cause of the higher Ru–La interaction in the supported $La_2O_3(50)–SiO_2$ solid.

The differences in thermal stability of the CO adsorbed species on Ru supported on silica or on binary $La_2O_3–SiO_2$ supports sustain that the presence of lanthanum influences the metal–support interaction and metal dispersion. On the other hand, the mild stability of the $Ru^0$–CO carbonyl groups on the $Ru/La_2O_3(40)–SiO_2$ is in agreement with the lowest metal–support interaction.

## Acknowledgements

The authors wish to acknowledge the financial support received from UNL and CONICET. Thanks are also given to ANPCyT for Grant PME 8 – 2003 to finance the purchase of the UHV Multi Analysis System, to the Japan International Cooperation Agency (JICA) for the donation of the major instruments used in this study, and to Prof. Elsa Grimaldi for the English language editing.

## References

[1] J.R. Rostrup-Nielsen, J.-H. Bak Hansen, J. Catal. 144 (1993) 38–49.
[2] U.L. Portugal, C.M. Marques, E.C. Araujo, E.V. Morales, M.V. Giotto, J.M.C. Bueno, Appl. Catal. A: Gen. 193 (2000) 173–183.
[3] P. Ferreira-Aparicio, L. Rodriguez-Ramos, J.A. Anderson, A. Guerrero-Ruiz, Appl. Catal. A: Gen. 202 (2000) 183–196.
[4] M. Bradford, M.A. Vannice, J. Catal. 183 (1999) 69–75.
[5] J. Wei, E. Iglesia, J. Phys. Chem. B 108 (2004) 7253–7262.
[6] K. Nagaoka, M. Okamura, K. Aika, Catal. Commun. 2 (2001) 255–260.
[7] F. Mark, W. Maier, J. Catal. 164 (1996) 122–130.
[8] S.M. Gheno, S. Damyanova, B.A. Riguetto, C.M.P. Marques, C.A.P. Leite, J.M.C. Bueno, J. Mol. Catal. A: Chem. 198 (2003) 263–275.
[9] N. Matsui, K. Anzai, N. Akamatsu, K. Nakagawa, N. Ikenaga, T. Suzuki, Appl. Catal. A: Gen. 179 (1999) 247–256.
[10] B. Faroldi, C. Carrara, E.A. Lombardo, L. Cornaglia, Appl. Catal. A: Gen. 319 (2007) 38–46.
[11] M. Safariamin, L.H. Tidahy, E. Abi-Aad, S. Siffert, A. Aboukaïs, C. R. Chim. (2009), doi:10.1016/j.crci.2008.10.021.
[12] J. Múnera, S. Irusta, L. Cornaglia, E. Lombardo, Appl. Catal. A: Gen. 245 (2003) 383–395.
[13] S. Irusta, J. Múnera, C. Carrara, E. Lombardo, L. Cornaglia, Appl. Catal. A: Gen. 287 (2005) 147–158.
[14] W.H. Casinelli, L. Feio, J.C.S. Araújo, C. Hori, F.B. Noronha, C.M. Marques, J.M.C. Bueno, Catal. Lett. 120 (2008) 86–94.
[15] Y. Cui, H. Zhang, H. Xu, W. Li, Appl. Catal. A: Gen. 331 (2007) 60–69.
[16] M. Bradford, M. Vannice, Catal. Rev. Sci. Eng. 41 (1999) 1–42.
[17] X. Shen, L.-J. Garces, Y. Ding, K. Laubernds, R. Zerger, M. Aindow, E. Neth, S. Suib, Appl. Catal. A: Gen. 335 (2008) 187–195.
[18] S. Yokota, K. Okumura, M. Niwa, Catal. Lett. 84 (2002) 131–134.
[19] H. Vidal, S. Bernal, R. Baker, D. Finol, J.A. Perez Omil, J.M. Pintado, J.M. Rodriguez Izquierdo, J. Catal. 183 (1999) 53–62.
[20] M.M.V.M. Souza, D.A.G. Aranda, C.A.C. Pérez, M. Schmal, Phys. Stat. Sol. (a) 187 (2001) 297–303.
[21] W. Grünert, U. Sauerlandt, R. Schlögl, H.G. Karge, J. Phys. Chem. 97 (1993) 1413–1419.

[22] G.R. Gallaher, J.G. Goodwin, C.S. Huang, M. Houalla, J. Catal. 140 (1993) 453–463.
[23] E.V. Makshina, S.V. Sirotin, M.W.E. van den Berg, K.V. Klementiev, V.V. Yushchenko, G.N. Mazo, W. Grünert, B.V. Romanovsky, Appl. Catal. A: Gen. 312 (2006) 59–66.
[24] Q.G. Yan, T.H. Wu, W.Z. Weng, H. Toghiani, R.K. Toghiani, H.L. Wan, C.U. Pittman Jr., J. Catal. 226 (2004) 247–259.
[25] H. Vidal, S. Bernal, R. Baker, G. Cifredo, D. Finol, J.M. Rodriguez Izquierdo, Appl. Catal. A: Gen. 208 (2001) 111–123.
[26] S. Bernal, G. Blanco, J. Calvino, M. Rodríguez-Izquierdo, H. Vidal, J. Alloys Compd. 250 (1997) 461–466.
[27] K. Hadjiivanov, J.C. Lavalley, J. Lamotte, F. Maugé, J. Saint-Just, M. Che, J. Catal. 176 (1998) 415–425.
[28] K. Hadjiivanov, G. Vayssilov, Adv. Catal. 47 (2002) 307–511.
[29] A.J. Marchi, Appl. Spectrosc. 4 (2002) 239–251.
[30] N.M. Gupta, V.S. Kamble, R.M. Iyer, K. Ravindranathan Thampi, M.J. Grätzel, J. Catal. 137 (1992) 473–486.
[31] C. Elmasides, D.I. Kondarides, W. Grünert, X.E. Verykios, J. Phys. Chem. B 103 (1999) 5227–5239.
[32] A. Fielicke, P. Gruene, G. Meijer, D.M. Rayner, Surf. Sci. 603 (2009) 1427–1433.
[33] G.H. Yokomizo, C. Louis, T. Bell, J. Catal. 120 (1989) 1–14.
[34] S. Lacombe, C. Geantet, C. Mirodatos, J. Catal. 151 (1994) 439–452.
[35] M.R. Goldwaser, M.E. Rivas, E. Pietri, M.J. Perez-Zurita, M.L. Cubeiro, A. Grivobal-Constant, G. Leclercq Goldwaser, J. Mol. Catal. A: Chem. 228 (2005) 325–331.
[36] J.M. Wei, E. Iglesia, J. Catal. 225 (1) (2004) 116–127.
[37] H.L. Abbott, I. Harrison, J. Catal. 254 (2008) 27–38.
[38] C. Carrara, J. Múnera, E.A. Lombardo, L.M. Cornaglia, Top. Catal. 51 (2008) 98–106.
[39] J.R. Rostrup-Nielsen, Science 308 (2005) 1421–1422.
[40] G. Jones, J.G. Jakobsen, S.S. Shim, J. Kleisa, M.P. Andersson, J. Rossmeisl, F. Abild-Pedersen, T. Bligaard, S. Helvegc, B. Hinnemann, J.R. Rostrup-Nielsen, I. Chorkendorff, J. Sehested, J.K. Nørskova, J. Catal. 259 (2008) 147–160.
[41] J.R. Rostrup-Nielsen, J. Sehested, J.K. Norskov, Adv. Catal. 47 (2002) 65–139.